A study on the effect of poro-visco-elasticity on the mechanical properties of pavement structure determined by Falling Weight Deflectometer Test

Ako Bahari[1], Ahmed Shalaby[2], Neil Popplewell[1], and Pooneh Maghoul[2]
[1]*Department of Mechanical Engineering, University of Manitoba, Winnipeg, Manitoba, Canada*
[2]*Department of Civil Engineering, University of Manitoba, Winnipeg, Manitoba, Canada*

ABSTRACT
Acquiring detailed information about the state of the pavement structures is an important element in rehabilitation planning of sections showing significant damage. The Falling Weight Deflectometer Test (FWD) is a popular Non-Destructive Testing (NDT) technique used to characterize the mechanical properties of a pavement structure. This paper aims to study the effect of poro-visco-elasticity of the pavement structure on the mechanical parameters such as the resilient modulus and structural damping as determined by FWD using a novel dynamic algorithm rather than a quasi-static analysis. For this purpose, a poro-visco-elastic Forward Solver Kernel was developed. The associated forward solver is cross-checked against viscoelastic and elastic limit cases.

RÉSUMÉ
Acquérir des informations détaillées sur l'état des structures de chaussée est un élément essentiel dans n'importe quel programme de réhabilitation pour les sections subites des dommages importants. L'essai de déflectomètre à masse tombante (FWD) est l'une des techniques d'essais non destructifs (NDT) les plus populaires dans la caractérisation des propriétés mécaniques de la structure de la chaussée. Cet article vise à étudier l'effet de poro-visco-élasticité de la structure de la chaussée sur les paramètres mécaniques tels que le module élastique ou réversible ainsi que l'amortissement structurel. Ces paramètres sont déterminés par FWD en utilisant un nouvel algorithme dynamique plutôt qu'une analyse quasi-statique. A cette fin, une solution analytique poro-viscoélastique est utilisée. La solution analytique associée est vérifiée en comparaison avec les solutions viscoélastique et élastique. Finalement, la fonction Green du system est évaluée.

1 INTRODUCTION

Pavement structures reach performance limits when there are multiple deteriorations caused by repeated vehicle loading and environmental effects. Due to the safety and comfort point of view, it is important to acquire detailed information about the state of the pavement structures. It is, in fact, an important element in rehabilitation planning of sections showing significant damage. FWD is one of the most widely accepted NDT approaches in evaluating pavement structure in terms of the strength and load baring capacity. The information provided by FWD are essential part in a cost effective maintenance framework in pavement structures.

Non-Destructive Testing (NDT) techniques have been broadly used for structural health monitoring and low-cost assessment in transportation. Among different NDT approaches, Falling Weight Deflectometer Test (FWD) is one of the most popular techniques in characterization of the mechanical properties of the pavement structure. The FWD test measures the surface deflections caused by dropping a known mass from a specific height onto a load plate placed on the pavement surface, and associated stress wave propagating through the multilayer pavement structure. Geophones are used to record the time histories of the vertical deflections of the pavement surface at various distances from the center of the load-plate.

Several wave types will propagate through soil layers and reflect and diffract at layer interfaces due to the impact excitation source used at the ground surface during a FWD test. Acquired surface displacement data are later used as the input of a back-calculation algorithm to inversely determine the mechanical properties of the layers constituting the multilayered flexible pavement system. The back-calculation algorithm consists of a forward solver (forward kernel) and an inverse scheme. The accuracy of the forward solver is the key to achieving better precision and reliability with the inversion scheme.

The current practical state-of-the-art of this technique is, mostly, limited to the quasi-static inversion of the maximum measured deflections. However, this approach does not take advantage of the additional information contained in the stress wave time histories such as damping, moisture content, and the effect of porous structure. The accuracy of determining the mechanical properties of the layers would also improve by using a comprehensive dynamic analysis rather than a quasi-static analysis.

The presence of moisture in the pavement structure can significantly affect the performance of the pavement. For example, an increase of 2% in optimum moisture content, would decrease the resilient modulus of the whole structure by as much as 75%. Another important issue to the pavement maintenance is the seasonal factor in cold regions. For example, the resilient modulus in winter is approximately on average 40% higher than the one in early spring (thawing season) (Ji et al., 2010).

The current state-of-the-art in FWD, using a quasi-static technique, cannot account for the presence of moisture in the subgrade. See, for example, Al-Khoury et al. (2001) and Lee (2014). Consequently, a more realistic hydro-mechanical dynamic model is needed to determine mechanical as well as hydraulic properties such as water content, porosity, and visco-elastic parameters.

This paper, first, aims to include the effect of moisture present in the pavement structure on its dynamic behavior which influences effective mechanical parameters such as the elastic or resilient modulus and structural damping. Subsequently a porous forward solver kernel is developed in time domain. Corresponding inversion algorithms for the Laplace and Hankel transforms are implemented and improved. Later, the temporal and spatial description of the loading is modified to better describe an actual falling weight impact. These modifications, significantly improve the computational efficiency while improving the accuracy at the same time. It is shown that this solver can be reduced to an equivalent elastic or viscoelastic one, as two subsequent limit cases.

2 MECHANICS OF WAVES IN A POROUS MEDIUM

A saturated porous medium is composed of a solid skeleton and a porous space filled with water. According to principles of continuum mechanics, any infinitesimal volume of a saturated porous medium can be considered as the superposition of two continua, skeleton continuum and fluid continuum, in time and space. The propagation of waves in a fluid-saturated porous solid is presented in this section in the framework of the theory of dynamic poro-elasticity, also known as Biot's theory (Biot, 1956:1,2).

Biot assumed a porous medium as macroscopically homogeneous and isotropic. Hence the material is described in terms of averaged field variables and material properties. The average macroscopic displacement of the solid skeleton and the saturating fluid, in the elementary macroscopic volume (EMV), are designated by the vectors u_i and U_i, respectively. The relevant physical parameters are listed as follows:

- β is the first Biot coefficient;
- m is the second Biot coefficient representing the macroscopic elastic coupling;
- λ, μ are the Lame constants of the solid skeleton;
- $\phi_0$is the porosity;
- K_0 is the bulk modulus of a dry skeleton, i.e., for an "open" system, $p_0 = 0$;
- K_s is the bulk modulus of the material constituting the elastic matrix;
- K_{fl} is the bulk modulus of the saturating fluid;
- K_f is the bulk modulus of the "closed" system;
- ρ_{11}, ρ_{12} and ρ_{22} are frequency independent effective densities;
- ρ_f is the density of the saturating fluid;
- ρ_s the density of solid particles;
- α_∞ is tortuosity (structure factor) of the porous medium;
- $K = k/\eta_d$ is the coefficient of permeability representing the macroscopic viscous coupling due to the relative motion between the Poiseuille-type flow and the solid matrix on the microscopic scale;
- η_d dynamic viscosity of a saturating fluid;
- k is the hydraulic conductivity;

For each homogeneous and isotropic layer, the above-mentioned parameters do not depend on the spatial coordinates.

2.1 Kinematic Assumptions

Kinematic assumptions include the infinitesimal deformations of the elastic skeleton,u_i, are subjected to the linearized Green-Cauchy strain tensor, ε_{ij}, so that

$$\varepsilon_{ij} = \tfrac{1}{2}\left(u_{i,j} + u_{j,i}\right). \quad [1]$$

Similarly, the strain tensor, e_{ij}, corresponding to fluid's particle displacement, U_i, becomes

$$e_{ij} = \tfrac{1}{2}\left(U_{i,j} + U_{j,i}\right). \quad [2]$$

Hence the second order deformation gradients are neglected.

2.2 Macroscopic Constitutive Equations

The constitutive equations for a fluid saturated porous medium based on the Biot theory is

$$\sigma_{ij} = \left(\lambda_f u_{i,i} + \beta M_0 w_{i,i}\right)\delta_{ij} + 2\mu\varepsilon_{ij} \quad [3a]$$

$$p = -M_0\left(w_{i,i} + \beta u_{i,i}\right) \quad [3b]$$

in which σ_{ij} and p are the macroscopic stress tensor and the mean pore fluid pressure, respectively. Moreover, $w_i = \phi_0(U_i - u_i)$ is the relative filtration displacement vector. The subscript $()_{,i}$ denotes a spatial derivative. Furthermore,

$$\lambda_f = K_f - 2\mu/3$$

$$K_f = \frac{\phi_0\left(\frac{1}{K_s} - \frac{1}{K_f}\right) + \frac{1}{K_s} - \frac{1}{K_0}}{\frac{\phi_0}{K_0}\left(\frac{1}{K_s} - \frac{1}{K_f}\right)}$$

$$M_0 = \frac{1}{\left(\frac{(\beta - \phi_0)}{K_f} + \frac{\phi_0}{K_f}\right)}$$

$$\beta = 1 - \frac{K_0}{K_s}. \quad [4]$$

(Johnson, et al. 1986) approximated this parameter as $\chi \approx 1/2$ for a medium consisting a set of non-intersecting tubes. Consequently, the viscous characteristic length $\Lambda \approx \sqrt{8\alpha\kappa/\phi_0}$, which exclusively depends on a frame geometry, has become as a widely accepted. It has been shown to be valid for a wide range of transport properties especially in soil dynamics.

2.3 Conservation of Linear Momentum

Conservation of the linear momentum for an elastic skeleton is

$$\sigma_{ij,j} + f_i = (1-\phi_0)\rho_s \ddot{u}_i + \phi\rho_f \ddot{U}_i \quad [5]$$

whereas for a saturating fluid, it becomes

$$p_{,i} = -\frac{\phi_0}{K} b(t) \otimes \left(\dot{U}_i - \dot{u}_i\right) + \rho_f(a_\infty - 1)\ddot{u}_i + \phi\rho_f \ddot{U}_i \quad [6]$$

where an overlying dot denotes a time derivative; f_i and $b(t)$ are body force and viscosity correction functions, respectively; $b(t)$ is a viscous coupling factor that accounts for the combined effects of macroscopic frictional dissipation due to the finite fluid viscosity (viscous drag forces) and the interaction between the fluid and solid movements (inertial forces). Furthermore, this factor describes the transition behavior from viscosity-dominated flow, of laminar type at low-frequency range, to inertia-dominated flow, of turbulent type at high-frequency range (Mesgouez et al., 2009). The closed form expression of this correction function in frequency domain is

$$b(\omega) = \sqrt{1 - i\,\chi\frac{\omega}{\omega_{JKD}}}, \quad \omega_{JKD} = \frac{\eta\,\phi_0}{\rho_f a_\infty k} \quad [7]$$

where ω_{JKD} is the radial frequency governing the viscous interaction transition regime which was proposed by (Johnson, et al. 1986). The effective damping changes when the viscous skin depth $\sqrt{2\eta/\rho_f\omega}$ becomes smaller than the pore size as the frequency increases beyond the characteristic frequency ω_{JKD}. Furthermore, χ is a dimensionless parameter accounting for a pore geometry.

2.4 Governing Equations' Assembly

By combining the kinematic assumptions, conservation of the linear momentum a long with the constitutive equations, the governing equations of the system emerges as

$$(\lambda + 2\mu)\ \boldsymbol{\nabla\nabla}.\boldsymbol{u} + Q\ \boldsymbol{\nabla\nabla}.\boldsymbol{U} - \mu\,\boldsymbol{\nabla}\times\boldsymbol{\nabla}\times\boldsymbol{u} = \rho_{11}\ddot{\boldsymbol{u}} + \rho_{12}\ddot{\boldsymbol{U}} + b(t)\otimes\left(\dot{\boldsymbol{u}} - \dot{\boldsymbol{U}}\right) \quad [8a]$$

$$Q\ \boldsymbol{\nabla\nabla}.\boldsymbol{U} + R\boldsymbol{\nabla\nabla}.\boldsymbol{U} = \rho_{11}\ddot{\boldsymbol{u}} + \rho_{12}\ddot{\boldsymbol{U}} + b(t)\otimes\left(\dot{\boldsymbol{u}} - \dot{\boldsymbol{U}}\right) \quad [8b]$$

in which $\boldsymbol{\sigma}$ is the Cauchy stress tensor. Furthermore

$\rho = \phi_0\rho_f + (1-\phi_0)\rho_s$; $\rho_{11} = \rho + \phi_0\rho_{fl}(\alpha_\infty - 2)$; $\rho_{12} = \phi_0\rho_f(1-\alpha_\infty)$; $\rho_{22} = \rho - \rho_{11} - 2\rho_{12} = \alpha_\infty\phi_0\rho_f$; $R = \phi_0^2 M_0$; $Q = \phi_0 M_0(\beta - \phi_0)$; $\lambda = \lambda_f + \phi_0 M_0(\phi_0 - 2\beta)$; $\beta = 1 - K/K_0$.

2.5 Helmholtz Decomposition

Resolution of the displacement field into two Helmholtz decomposition theorem allows us to resolve the solid and relative displacement fields as superposition of longitudinal and transverse vector components as follows,

$$\boldsymbol{u} = \boldsymbol{\nabla}\phi + \boldsymbol{\nabla}\times\boldsymbol{\psi} \text{ and} \quad [9a]$$
$$\boldsymbol{w} = \boldsymbol{\nabla}\chi + \boldsymbol{\nabla}\times\boldsymbol{\theta}\,, \quad [9b]$$

where ϕ and χ are the scalar compressional wave potentials and $\boldsymbol{\psi}$ and $\boldsymbol{\theta}$ are the vectorial shear wave potentials. For the uniqueness of the solution the following Gauge conditions shall be satisfied as

$$\boldsymbol{\nabla}.\boldsymbol{\psi} = 0, \quad \boldsymbol{\nabla}.\boldsymbol{\theta} = 0. \quad [10]$$

This condition ensures the *equivoluminal* shear motion. Substituting Eqs. (9a) and (9b) into Biots' field equations of motion, Eqs. (8a) and (8b), we obtain two sets of uncoupled partial differential equations relative, respectively, to compressional waves P1 and P2 connected to Helmholtz scalar potentials ϕ and χ, and to shear wave S connected to Helmholtz vector potentials $\boldsymbol{\psi}$ and $\boldsymbol{\theta}$ as follows, in the Laplace domain with zero initial conditions

$$\begin{pmatrix}\lambda+2\mu & Q\\ Q & R\end{pmatrix}\begin{pmatrix}\nabla^2\phi\\ \nabla^2\boldsymbol{\psi}\end{pmatrix} = \begin{pmatrix}-\rho_{11}s^2 + sb & -\rho_{12}s^2 - sb\\ -\rho_{12}s^2 - sb & -\rho_{22}s^2 + sb\end{pmatrix}\begin{pmatrix}\nabla^2\phi\\ \nabla^2\boldsymbol{\psi}\end{pmatrix} \quad [11]$$

$$\begin{pmatrix}\mu & 0\\ 0 & 0\end{pmatrix}\begin{pmatrix}\nabla^2\phi^r\\ \nabla^2\boldsymbol{\psi}^r\end{pmatrix} = \begin{pmatrix}-\rho_{11}s^2 + sb & -\rho_{12}s^2 - sb\\ -\rho_{12}s^2 - sb & -\rho_{22}s^2 + sb\end{pmatrix}\begin{pmatrix}\nabla^2\chi\\ \nabla^2\boldsymbol{\theta}\end{pmatrix}. \quad [12]$$

Using standard methods of wave analysis, the above systems may be manipulated to yield Helmholtz equations:

$$\nabla^2\phi_{f,s} - k_{f,s}^2\phi_{f,s} = 0 \quad [13a]$$

$$\nabla^2\boldsymbol{\psi}_{f,s} - k_t^2\boldsymbol{\psi}_{f,s} = 0 \quad [13b]$$

where k_f, k_s and k_t denote the wave numbers of the fast compressional, slow compressional, and the elastic shear waves, respectively, in Laplace domain. They are defined as

$$k_{fs}^2 = \frac{Bm\sqrt{B^2 - 4AC}}{2A}$$
$$k_t^2 = \frac{C}{\mu(-\rho_{22}s^2 - sb)} \quad [14]$$

where

$$A = (\lambda + 2\mu)R - Q^2$$
$$B = \omega^2(\rho_{11}R + \rho_{22}(\lambda + 2\mu) - 2\rho_{12}Q) - \omega b(\lambda + 2\mu + 2Q + R)$$
$$C = \omega^2(\omega^2(\rho_{11}\rho_{22} - \rho_{12}^2) - s\rho b) \quad [15]$$

Next by introducing Eqs. (9) into (8), with some manipulations, the potentials $\phi, \chi, \boldsymbol{\theta}$ and $\boldsymbol{\psi}$ can be expressed as $\phi = \phi_f + \phi_s$, $\chi = \mu_f\phi_f + \mu_s\phi_s$ and $\boldsymbol{\theta} = \alpha_0\boldsymbol{\psi}$ where

$$\mu_{fs} = \frac{-s^2(\rho_{11}R - \rho_{12}Q) - k_{fs}^2\left((\lambda+2\mu)RQ^2\right) - s\,b(Q+R)}{-s^2(\rho_{22}Q - \rho_{12}R) - sb(Q+R)}$$

$$\alpha_0 = -\frac{sb + s^2\rho_{12}}{s^2\rho_{22} + s\,b} \quad [16]$$

Gauge condition leads only to independent shear wave potentials. The loading symmetry of problem in circumferential direction, also, leads to reduction of another shear wave potential. Consequently, only one scalar shear wave potential remain as, ψ. By substituting U_i with $u_i + w_i/\phi_0$ in equations (11) and (12) along with applying the resolution of equation (9), alternatively, the system of wave equations can be reduced into

$$[M]\begin{bmatrix}\ddot{\phi}\\ \ddot{\phi}^r\end{bmatrix} + [C]\begin{bmatrix}\dot{\phi}\\ \dot{\phi}^r\end{bmatrix} - [K_p]\begin{bmatrix}\nabla^2\phi\\ \nabla^2\phi^r\end{bmatrix} = \begin{bmatrix}0\\0\end{bmatrix} \quad [17a]$$

$$[M]\begin{bmatrix}\ddot{\psi}\\ \ddot{\psi}^r\end{bmatrix} + [C]\begin{bmatrix}\dot{\psi}\\ \dot{\psi}^r\end{bmatrix} - [K_s]\begin{bmatrix}\nabla^2\psi\\ \nabla^2\psi^r\end{bmatrix} = \begin{bmatrix}0\\0\end{bmatrix} \quad [17b]$$

where

$$[M] = \begin{bmatrix}(1-\phi)\rho_s + \phi\rho_f & \rho_f\\ \rho_f & a\rho_f/\phi\end{bmatrix},$$
$$[K_P] = \begin{bmatrix}(\lambda+\mu+m\beta^2) & m\beta\\ m\beta & m\end{bmatrix},$$
$$[K_S] = \begin{bmatrix}\mu & 0\\ 0 & 0\end{bmatrix} \text{ and}$$
$$[C] = \begin{bmatrix}0 & 0\\ 0 & \frac{1}{K}b(t)\otimes\end{bmatrix}. \quad [18]$$

The solution to the wave equations (12) are treated in two different ways and then their performance in terms of computational costs for the same accuracy is compared. These two methods differ in the way they treat the radial coordinate: in the first one a Hankel transform is used while in wave potentials are relaxed at a large distance form the loading center. However in both approaches a Laplace transform is applied to the time coordinate.

2.6 Double Transformed Solution

The solution of the wave potentials can be more conveniently treated if a double Laplace ($t \to s$)

$$\mathcal{L}\{\theta(t)\} = \hat{\theta}(s) = \int_{\gamma-i\infty}^{\gamma+i\infty} \theta(t)e^{-st}\,dt \quad [19]$$

and Hankel transform ($r \to \zeta$) applied to equations of (17a) and (17b) as

$$\hat{\theta}(\zeta) = \int_0^\infty \theta(r)J_p(\zeta\, r)\zeta\, d\zeta\,. \quad [20]$$

Hence that $\mathcal{L}\{\mathrm{a(t)} \otimes \mathrm{b(t)}\} = s\,\bar{a}\,(s)\,\bar{b}(s)$ if the system is at rest initially at $t = 0$. conditions are zero. Subsequently, the equation (17) turns into

$$\left(\left(\zeta^2 - \frac{d^2}{dz^2}\right)[K_p] + s^2[M] - s[C]\right)\begin{pmatrix}\hat{\phi}\\ \hat{\phi}^r\end{pmatrix} = \begin{pmatrix}0\\0\end{pmatrix} \quad [21a]$$

And

$$\left(\left(\zeta^2 - \frac{d^2}{dz^2}\right)[K_s] + s^2[M] - s[C]\right)\begin{pmatrix}\hat{\psi}\\ \hat{\psi}^r\end{pmatrix} = \begin{pmatrix}0\\0\end{pmatrix}. \quad [21b]$$

Solution of the second order above mentioned system of equations, simply, will be periodic in the z direction, such that

$$\begin{pmatrix}\hat{\phi}\\ \hat{\phi}^r\end{pmatrix} = A_1^{inc}\begin{pmatrix}1\\ B_1\end{pmatrix}e^{-k_{p_1}s} + A_1^{ref}\begin{pmatrix}1\\ B_1\end{pmatrix}e^{-k_{p_1}s} + A_2^{inc}\begin{pmatrix}1\\ B_2\end{pmatrix}e^{-k_{p_1}s} + A_2^{ref}\begin{pmatrix}1\\ B_2\end{pmatrix}e^{-k_{p_1}s} \quad [22]$$

where

$$B_i = -\frac{\left(k_{p_i}^2 + \zeta^2\right)\alpha M + s^2\rho_f}{\left(k_{p_i}^2 + \zeta^2\right)M + \frac{s^2\rho_f\alpha_\infty}{\phi_0} - s\frac{b(s)}{K}} \quad [23]$$

in which i refers to a layer and its material properties. A_i^{inc} and A_i^{ref} are unknown coefficients. These wave potentials are related to displacements through the Helmholtz decomposition of equation (10). Then the displacements are transferred to strains elements through Green-Cauchy equations (1) and (2). Finally, the stress elements can be retrieved by using the constitutive equations (3).

Next by enforcing the continuity of layer through the displacement (u_r, u_z) and stress (σ_{zz}, σ_{rz}) elements, those unknown coefficients are determined. Indeed a local transfer matrices for bounded and half space layers are constructed first. A global stiffness matrices is assembled following equations (11), (12) and (13) in Kausel and Roesset (1981) in a way to swap these unknown coefficients with the interface displacements and stresses. A similar procedure is followed by Mesgouez and Mesgouez (2009) but by using a triple Fourier transform in Cartesian coordinates x and y as well as in time t rather than a joint Laplace and Hankel transforms. Inversion schemes for these double transform is explained next.

2.6.1 Inversion of the Transformed Solutions

A zero order and first order Hankel transforms of the first kind are used to transform the vertical and radial displacements, respectively. Therefore, the inverse Hankel transform of respective orders must be carried out for the two displacements. A numerical integration scheme is adopted here which was originally proposed by (Cornille, 1972). An inverse Hankel transform of p^{th} order can be defined as

$$u(r) = \int_0^\infty \hat{u}(\zeta)J_p(\zeta\, r)\zeta\, d\zeta \quad [25]$$

where $J_p(\zeta)$ is the p-th order Bessel function of first kind. This integral can be broken down to multiple intervals of ζ, such as that

$$u(r) = \int_0^{\infty} \hat{u}(\zeta) J_p(\zeta\, r)\zeta\, d\zeta = \int_{b_1}^{b_2} \hat{u}(\zeta) J_p(\zeta\, r)\zeta\, d\zeta + \int_{b_2}^{b_3} \hat{u}(\zeta) J_p(\zeta\, r)\zeta\, d\zeta + \int_{b_3}^{b_4} \hat{u}(\zeta) J_p(\zeta\, r)\zeta\, d\zeta + \cdots \quad [26]$$

where b_i are the zeros of Bessel function $(p+1)$-th kind of the first order, $J_{p+1}(b_i) = 0$ (). Each of the sub-integrals should be evaluated by dividing $[b_i, b_{i+1}]$ to ten sub integrations as well to achieve a reasonably stable numerical convergence (Cornille, 1972). Each of those intervals are integrated by a Gaussian Quadrature approach with ten nodes which corresponds to a degree of exactness of 17. A Gauss-Lobatto Quadrature is chosen since it includes the nodes on the boundary as well. This integration scheme is outlined for an arbitrary interval of $[a, b]$. First the abscissa are the root of $P_{n-1}{}'(y_i) = 0$, where $P_n(x)$ is the associated Legendre function of the $n-$th order. Then these nodes are normalized to [-1,1] by $x_i = \frac{b-a}{2} y_i + \frac{b+a}{2}$. The corresponding weights are

$$w_1 = w_n = \frac{2}{n\,(n-1)}, \quad w_i = \frac{2}{n\,(n-1)\;P_{n-1}{}'(y_i)^2}, \quad [27]$$

Finally, this integration formula can be written in closed-form as

$$\int_a^b f(x)dx = \frac{b-a}{2}\int_{-1}^{1} f\left(\frac{b-a}{2}y + \frac{b+a}{2}\right)dy \approx \frac{b-a}{2}\left(w_1 f(a) + w_n f(b) + \sum_{i=2}^{n-1} w_i f(x_i)\right) = \frac{b-a}{2}\left(w_1 f(a) + w_n f(b) + \sum_{i=2}^{n-1} w_i f\left(\frac{b-a}{2}y_i + \frac{b+a}{2}\right)\right) \quad [28]$$

where $n = 10$.

The Laplace inverse transform of an arbitrary function is carried on by using a Fourier series based approach due to Durbin (Abate and Valko, 2004). The linear operators of Laplace transform and its subsequent complex inversion can be defined, respectively, as

$$\mathcal{L}^{-1}\{\theta(t)\} = \theta(s) = \int_0^{\infty} \tilde{\theta}(s) e^{st}\, dt \quad [29]$$

γ is an arbitrary real number greater than the real parts of all singularities of $\theta(s)$.

$$\tilde{\theta}(t) \approx \tfrac{1}{2}c_0(t) + \textstyle\sum_{n=1}^{N} c_n(t), \qquad t \in [0, T] \quad [30]$$

where $c_n(t) = (e^{\gamma t}/T)Re\{e^{i\,n\pi\,t/T}\theta(\gamma + i\,n\,\pi/T)\}$. The convergence rate is enhanced through a ***Lanzo's*** filter. The second method of solving equations (17) is briefly discussed next.

2.7 Relaxed Potential Solution

The rational here is that all wave function are set to zero at $r = r_\infty$ so there is no reflections in the radial direction instead of a Hankel transform. Compressional waves are expressed in terms of the zero order Bessel functions of the first kind, $J_0(z)$, while the shear waves are defined by the first order Bessel functions of the first kind, $J_1(z)$. Consequently following characteristic equations form as

$$J_0(k_m^P r_\infty) = 0, \quad m = 1,2,\ldots \quad [31a]$$

in the case of compressional waves, whereas

$$J_1(k_m^S r_\infty) = 0, \quad m = 1,2,\ldots \quad [31b]$$

k_m are determined by solving to latter equations. As the characteristic equation for shear waves. Obviously each k_m corresponds to m-th vibratory mode. A similar approach was taken by Al-Khoury, et al (2001 and 2007) multilayered system. However shear wave modes corresponding k_m^S were not included in the construction of the final total solution through the assembly of the transfer and global stiffness matrices. The global stiffness matrix is developed in a similar way as the pervious subsection.

2.8 Excitation Characteristics Modification

Description of the loading is modified in order to better including characteristics of an actual impact at the surface. Cauchy's traction stress vector is defined as $\boldsymbol{t}_n = \boldsymbol{\sigma}_n.\boldsymbol{n}_z$, where $\boldsymbol{n}_z = -\boldsymbol{e}_z$ is perpendicular to the surface and points outwards. In case of pure normal loading, a surface traction force can be decomposed to temporal and spatial components such that

$$\sigma_{zz}(t, r, z=0) \equiv -F(r,z) = -f_t(t)\begin{cases} f_r(r), & 0 < r < r_0 \\ 0, & r > r_0 \end{cases} \quad [32]$$

where r_0 is the radius of a circular impactor. Furthermore $f_t(t)$ is the time dependency of an excitation. Discussions are made to improve the accuracy and numerical stability of these two parts separately.

2.8.1 Spatial Description of the Impact

Spatial description of a load can be described in terms of the vibratory modes of the system as Fourier-Bessel series, such that

$$f_r(r) = \sum_{m=1}^{\infty} F_m J_0(k_m^P r). \qquad [33]$$

where

$$F_m = \frac{2}{r_\infty^2\, k_m^P\, J_1^2\left(r_\infty k_m^P\right)} \int_0^{r_\infty} r f_r(r) J_0(k_m^P\, r) dr. \qquad [34]$$

Pervious publications assumed a distribution, such that,

$$F_m = \frac{2\, r_0\, J_1(r_0 k_m^P)}{r_\infty^2\, k_m^P\, J_1^2(r_\infty k_m^P)}. \qquad [35]$$

This simplified assumption, however, is far from the actual distribution. This can be improved by applying a Hertzian contact force description of a cylinder over a half space within the elastic domain. This distribution is reported by Sneddon (1965) as

$$f_r(r) = \frac{1}{\sqrt{1 - \left(\frac{r}{r_0}\right)^2}}. \qquad [36]$$

The corresponding modal component by inserting the latter equation in equation (19), in closed-form, becomes

$$F_m = \frac{2\, r_0\, sin(r_0 k_m^P)}{r_\infty^2\, k_m^P\, J_1^2(r_\infty k_m^P)}. \qquad [37]$$

In the case of the dual transform approach, the Hankel transformed of this distribution turns into

$$\hat{f}_r(\zeta, s) = \frac{r_0}{\zeta} J_1(\zeta\, r_0) \qquad [38]$$

for uniform distribution while it becomes

$$\hat{f}_r(\zeta, s) = \sqrt{\rho^2}\, \frac{e^{i\zeta\rho}}{i\zeta} \qquad [39]$$

For the Hertzian contact model. The Fourier-Bessel series in equation (33) has an extremely slow convergence rate as reported by Al-Khoury, et al. (2001) and (2007). They used $M = 1700$ terms (modes) to get to a somehow acceptable convergence. We are proposing the implementation of a Cesearo summation approach, which is basically a filter. See, for example, Zhang and Geers (1993). The convergence rates of the classical versus the current proposed approach for a uniform distribution assumption a uniform distribution is depicted in Figure 1. Three truncation numbers of $M = 500, 1000$ and 1700 are considered. The convergence rate of the proposed method is very good even in 500 modes while the classical one struggles even with 1700 modes. This observation is augmented even further in the case of Hertzian distribution of the contact force as illustrated in the Figure 2.

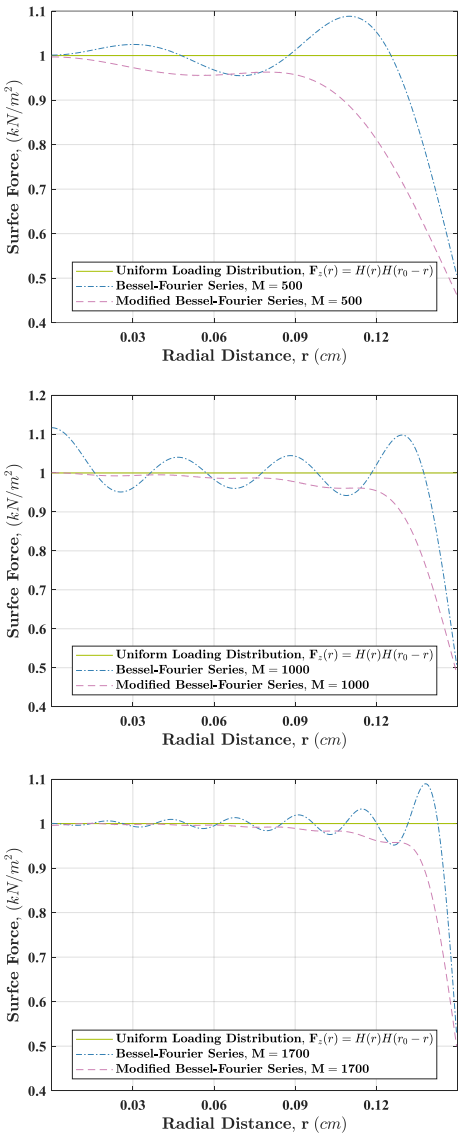

Figure 1. Convergence behavior of uniform distribution by using classical vs improved Ceasaro summation for different number of modes.

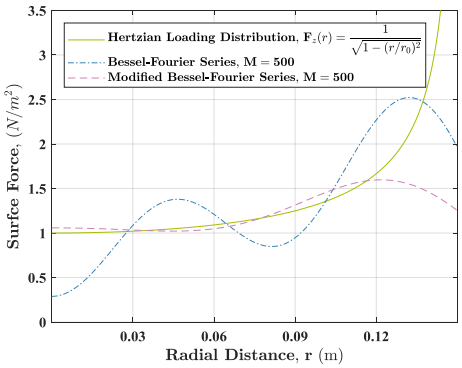

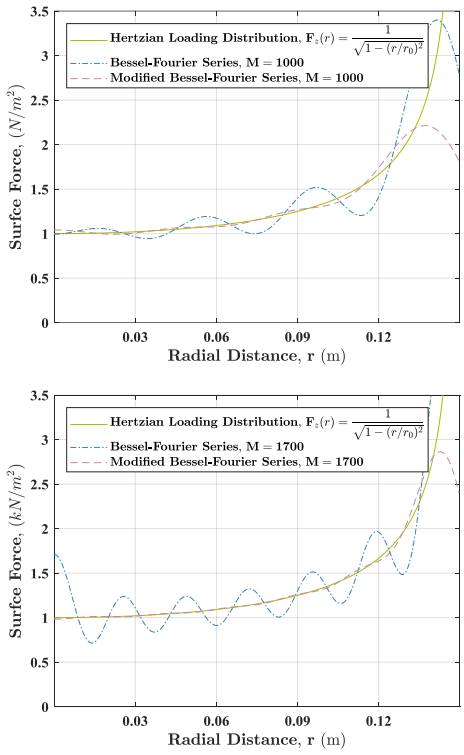

Figure 2. Convergence behavior of Hertzian distribution by using classical vs improved Ceasaro summation for different number of modes.

2.8.2 Temporal Description of the Excitation

For the particular application of the FWD, the temporal behavior of the load is described by a truncated half sine wave. See, for example, Al-Khoury, et al. (2001) and Lee (2014). However the discontinuities at the beginning and end of the half sine are nonphysical. Furthermore they lead to a numerical convergence issue for inversion back to time domain. There are some more physical alternatives which address those issues. A Gaussian pulse, for example, has a continuous and smooth temporal behavior which fits better to an actual excitation due to an impact load. The temporal expression of the pulse is

$$f_t(t) = e^{-\frac{(t-t_0)^2}{2\,{t_G}^2}} \qquad [24]$$

where in Laplace domain becomes

$$\tilde{f}_t(s) = \mu_{17}\, e^{s^2\mu_{20} - s\,t_{G0}}\; Erfc\left(\frac{s\,{t_{G\omega}}^2 - t_{G0}}{\mu_{19}}\right).$$

Time history of a Gaussian pulse is depicted in Figure 3 for $t_{G\omega} = \frac{1}{20}$, $t_{G0} = \frac{1}{5}$. This modification leads to much less numbers of required terms N in Laplace inversion, from 700 to as low as 200 terms.

3 VISCOELASTIC AND ELASTIC LIMIT CASES

By having the porosity $\phi_0 \to 0$, the $b(t) \to 1$and the governing equation (6b) disappears while (6b) turns into

$$(\lambda + 2\mu)\;\boldsymbol{\nabla\nabla}.\boldsymbol{u} - \mu\,\boldsymbol{\nabla}\times\boldsymbol{\nabla}\times\boldsymbol{u} = \rho_s\ddot{\boldsymbol{u}} \qquad [25]$$

which is the well-known Navier equation for the elastic wave propagation. If the Lame constants taken as functions of time, $\lambda = \lambda(t)$ and $\mu = \mu(t)$, the viscoelastic version of Navier equation appears, such that

$$(\lambda(t) + 2\mu(t)) \;*\; \boldsymbol{\nabla\nabla}.\boldsymbol{u} - \mu\,(t) * \boldsymbol{\nabla}\times\boldsymbol{\nabla}\times\boldsymbol{u} = \rho_s\ddot{\boldsymbol{u}} \qquad [26]$$

Where $*$ b represents the Stieltjes convolution which may be expressed as

$$f * g = \int_0^t f(t-\tau)\,\frac{\partial}{\partial\tau}g(\tau)\,d\tau\,.$$

See, for example, Rizzi (1989). This operator, in Laplace domain deconvolves. Subsequently, under zero initial conditions, it becomes $s\,\bar{f}(s)\,\bar{g}(s)$.

This brief limit-case discussion shows that the computer code based on the presented porous model, easily can be transformed to a fully elastic or viscoelastic one by setting the porosity ratio as very small value and some changes in Lame parameters.

4 A NUMERICAL CASE STUDY

Considering some interesting features of the frequency spectrum of Ricker impulse, in order to check the robustness of our code a case study is performed on this pulse. This Pulse is illustrated in Figure 3 with similar constants of Gaussian pulse. Two layered system with a bed rock considered in which the thickness of layers is $15cm$ and $25cm$. These numbers are chosen to have a stronger reflection form to the surface instead of dissipating wave into half space. A snapshot of the surface displacement is shown in Figure 4 at $r = 10\ cm$. The arrival of the longitudinal wave is followed by head waves which finally continues with the Reighley and shear waves. Normal displacement response u_z to this Ricker pulse at the loading center of $r = 0$ is illustrated in Figure 2.

5 CONCLUSIONS

A semi-analytical solution was implemented for a multi-layered formation. The layers are considered to be porous which were fully saturated with fluid; partial saturation condition cannot be treated by the proposed solution. The response of the system due to a surface traction is obtained in the transformed domain. Appropriate Laplace and Hankel inverse transform algorithms are utilized to retrieve the response in the time and space domain. This can serve as a forward solver for an inversion procedure which aims in evaluating the material properties of the layered system of a pavement non-destructively. The current improved forward solver enables us to target additional mechanical properties such as porosity and water content of the layered system in comparison with the previously applied constitutive models for fully elastic or viscoelastic models. Further investigations are in progress in implementing an inversion algorithm which works with porous forward kernel. The current forward solver handles

a fully saturated or completely dry conditions. Partial saturation becomes a nonlinear system which requires completely a different treatment. This can be, also, the subject of further improvements in the corresponding forward solver.

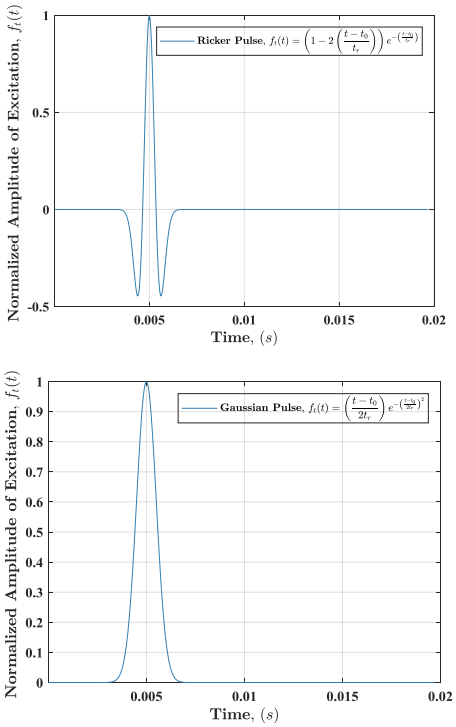

Figure 3. Time histories of proposed excitation functions, $f_t(t)$.

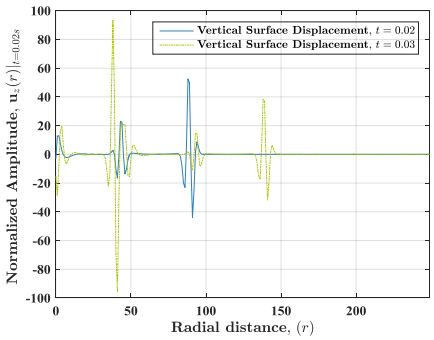

Figure 4. Displacement, $\boldsymbol{u_z}$, snapshots at $\boldsymbol{t = 0.02}$ and $\boldsymbol{0.03\ s}$.

6 REFERENCES

Biot MA. Theory of propagation of elastic waves in a fluid-saturated porous solid. I—Low-frequency range. The Journal of the Acoustical Society of America 1956; 28(2):168–178.

Biot MA. Theory of propagation of elastic waves in a fluid-saturated porous solid. II—Higher frequency range. The Journal of the Acoustical Society of America 1956; 28(2):179–191.

Sneddon, I. N. (1965). The relation between load and penetration in the axisymmetric Boussinesq problem for a punch of arbitrary profile. International journal of engineering science, 3(1), 47-57.

Kausel, E., & Roesset, J. M. (1981). Stiffness matrices for layered soils. Bulletin of the seismological Society of America, 71(6), 1743-1761.

Mesgouez A, Lefeuve-Mesgouez G. Study of transient poroviscoelastic soil motions by semi-analytical and numerical approaches. Soil Dynamics and Earthquake Engineering 2009; 29(2):245–248.

Al-Khoury, R., et al. "Spectral element technique for efficient parameter identification of layered media. I. Forward calculation." *International Journal of Solids and Structures*38.9 (2001): 1605-1623.

Al-Khoury, R., and L. J. Sluys. "A computational model for fracturing porous media." *International journal for numerical methods in engineering* 70.4 (2007): 423-444.

Abate, J. and Valko, P.P., 2004. Multi-precision Laplace transform inversion. International Journal for Numerical Methods in Engineering, 60, 979–993.

Ji, Y., Siddiki, N., Nantung, T., Kim, D. 2010. Effect of moisture variation on subgrade and base material Mr design values and its implementation in MEPDG. FWD User's Group Meeting.

Rizzi, S., 1989. A spectral analysis approach to wave propagation in layered media. Dissertation (PhD). Purdue University.

Mesgouez, A., and Lefeuve-Mesgouez, G. 2009. Transient solution for multilayered poroviscoelastic media obtained by an exact stiffness matrix formulation. Int. J. Numer. Anal. Meth. Geomech. 2009; 33:1911-1931.

Bourbie, T., Coussy, O., and Zinszner, B. E. 1987. Acoustics of porous media, Gulf Publishing, Houston.

Allard, J. F. 1993. Propagation of sound in porous media, modeling sound absorbing materials, Elsevier Applied Science, London.

Johnson, D. L., Koplik, J., and Dashen, R. 1987. "Theory of dynamic permeability and tortuosity in fluid-saturated porous media." J. Fluid Mech., 76, 379–402.

Cornille, P., 1972. Computation of Hankel transforms. SIAM Review, 14 (2), 278–285.

Zhang, Peizhen, and Thomas L. Geers. "Excitation of a fluid-filled, submerged spherical shell by a transient acoustic wave." The Journal of the Acoustical Society of America 93, no. 2 (1993): 696-705.